Key Points:

Correspondence to:
E. Aa,
aercha@mit.edu

Multi-Instrument and SAMI3-TIDAS Data Assimilation Analysis of Three-Dimensional Ionospheric Electron Density Variations During the April 2024 Total Solar Eclipse

Ercha Aa[1] , **Joseph Huba**[2] , **Shun-Rong Zhang**[1] , **Anthea J. Coster**[1], **Philip J. Erickson**[1] , **Larisa P. Goncharenko**[1] , **Juha Vierinen**[3] , and **William Rideout**[1]

[1]Haystack Observatory, Massachusetts Institute of Technology, Westford, MA, USA, [2]Syntek Technologies, Fairfax, VA, USA, [3]Department of Physics and Technology, The Arctic University of Norway, Tromsø, Norway

Abstract This paper conducts a multi-instrument and data assimilation analysis of the three-dimensional ionospheric electron density responses to the total solar eclipse on 08 April 2024. The altitude-resolved electron density variations over the continental US and adjacent regions are analyzed using the Millstone Hill incoherent scatter radar data, ionosonde observations, Swarm in situ measurements, and a novel TEC-based ionospheric data assimilation system (TIDAS) with SAMI3 model as the background. The principal findings are summarized as follows: (a) The ionospheric hmF2 exhibited a slight enhancement in the initial phase of the eclipse, followed by a distinct reduction of 20–30 km in the recovery phase of the eclipse. The hmF2 in the umbra region showed a post-eclipse fluctuation, characterized by wavelike perturbations of 10–25 km in magnitude and a period of ~30 min. (b) There was a substantial reduction in ionospheric electron density of 20%–50% during the eclipse, with the maximum depletion observed in the F-region around 200–250 km. The ionospheric electron density variation exhibited a significant altitude-dependent feature, wherein the response time gradually delayed with increasing altitude. (c) The bottomside ionospheric electron density displayed an immediate reduction after local eclipse began, reaching maximum depletion 5–10 min after the maximum obscuration. In contrast, the topside ionospheric electron density showed a significantly delayed response, with maximum depletion occurring 1–2.5 hr after the peak obscuration.

Plain Language Summary On 8 April 2024, a total solar eclipse traversed across North America with a dense network of observational equipment in place, providing a great opportunity for analyzing ionospheric effects during the eclipse. This paper presents a multi-instrument and data assimilation analysis of the three-dimensional ionospheric electron density response to this solar eclipse, utilizing Millstone Hill incoherent scatter radar data, ionosonde observations, Swarm satellite in situ measurements, and a new TEC-based ionospheric data assimilation system (TIDAS) over continental US and adjacent regions with the SAMI3 as the background model. The observations and SAMI3-TIDAS data assimilation reveals the time-evolving 3-D spatial distribution of the ionospheric electron density during the eclipse, highlighting key features of altitude-dependent ionospheric variation with significant discrepancies and time delays between the bottomside and topside ionosphere.

1. Introduction

A solar eclipse represents not only a remarkable astronomical phenomenon but also offers a unique natural experiment within the geospace system for investigating various ionospheric responses to transient changes in solar irradiation. During an eclipse, a sharp decrease in solar irradiation leads to sudden reductions in both photo-ionization and solar extreme ultraviolet (EUV) heating in the upper atmosphere, which create localized depletion in ionospheric electron densities and cooling of plasma temperatures (e.g., Afraimovich et al., 1998; MacPherson et al., 2000; Rishbeth, 1968). Furthermore, the decrease in plasma temperature and pressure can reduce the plasma equilibrium scale height, consequently increasing the downward plasma diffusion in the F2 and topside iono-sphere (Evans, 1965; Jakowski et al., 2008). Moreover, the eclipse-induced atmospheric cooling can cause thermospheric wind disturbances and composition changes near the totality region, thereby altering the neutral dynamics and electrodynamics in the Ionosphere-Thermosphere system (Aa et al., 2020; Aryal et al., 2020; St.-Maurice et al., 2011; Tomás et al., 2007). Additionally, the immediate changes in atmospheric temperature and pressure gradient initiated by the moon's shadow lead to the generation of certain gravity waves, bow waves, and traveling ionospheric disturbances (TIDs) (Aa et al., 2021; Chimonas, 1970; Gómez, 2021; Liu et al., 2011; Zhang

et al., 2017). Overall, a solar eclipse can generate complex ionospheric effects across diverse spatial and temporal scales, resulting from the interaction of the aforementioned photo-chemical, diffusion, neutral winds, composition, and electrodynamical processes. Thus, the impacts of solar eclipses on the ionosphere have been extensively studied using multi-instrumental observations and numerical simulations (G. Chen et al., 2013; Coster et al., 2017; Ding et al., 2010; Farges et al., 2001; Goncharenko et al., 2018; Huang et al., 2020; Huba & Drob, 2017; Jonah et al., 2020; Le et al., 2009; Müller-Wodarg et al., 1998; Salah et al., 1986; Silwal et al., 2021).

Our understanding of the solar eclipse effects on geospace system has been largely advanced through extensive community-wide studies on the 2017 Great American solar eclipse facilitated by the abundance of available data, such as ionosonde measurements (Reinisch et al., 2018), incoherent scatter radar observations (Goncharenko et al., 2018), Global Navigation Satellite Systems (GNSS) total electron content (TEC) data (Cherniak & Zakharenkova, 2018; Coster et al., 2017; Liu et al., 2020; Zhang et al., 2017, 2021), amateur radio sounding measurements (Frissell et al., 2018), and satellite observations (Hairston et al., 2018; Mrak, Semeter, Nishimura, et al., 2018; Perry et al., 2019; Yau et al., 2018). Moreover, numerical simulations have been widely used to investigate the ionosphere-thermosphere response (C.-H. Chen et al., 2019; Cnossen et al., 2019; Dang et al., 2018; Huba & Drob, 2017; Lei et al., 2018; Wang et al., 2019; Wu et al., 2018). Observational and modeling studies made in this eclipse have collectively revealed a number of interesting phenomena, such as large-scale ionospheric variations in TEC and electron densities (Aa et al., 2023; C. H. Chen et al., 2022; Cherniak & Zakharenkova, 2018; Coster et al., 2017; He et al., 2018; Lin et al., 2023; Tian et al., 2022), atmospheric gravity waves and bow waves (Harding et al., 2018; Lin et al., 2018; Nayak & Yiğit, 2018; Pradipta et al., 2018; Sun et al., 2018; Verhulst & Stankov, 2018; Yan et al., 2021; Zhang et al., 2017), TIDs related to eclipse and/or non-eclipse sources (Aryal et al., 2019; Eisenbeis et al., 2019; Mrak, Semeter, Nishimura, et al., 2018), ionospheric plasma temperature and drift responses (Goncharenko et al., 2018; Hairston et al., 2018), topside ionospheric disturbances (Perry et al., 2019; Yau et al., 2018), conjugate ionospheric changes (Huba & Drob, 2017; Zhang et al., 2021), and neutral atmospheric responses (Cnossen et al., 2019; Dang et al., 2018; Lei et al., 2018; Wang et al., 2019; Wu et al., 2018).

Despite the substantial progress achieved in previous studies, there remain some critical issues that need further addressing, as outlined below.

1. Specifying the three-dimensional (3-D) ionospheric electron density (Ne) responses to a solar eclipse has always been a critical yet a challenging issue. The horizontal features of ionospheric morphology have been extensively studied using integrated TEC from ground-based GNSS measurements. However, an eclipse can also induce significant and complex variations in the vertical domain of the ionosphere: essential information about ionospheric altitudinal structures is absent in 2-D TEC maps. The altitudinal variation of the ionosphere is crucial for providing distinctive insights into the modification of ionospheric thermal state and dynamics during an eclipse, such as plasma scale height and vertical motion. From an observational point of view, the incoherent scatter radar is a powerful instrument for measuring the ionosphere with full altitude profiles, capable of revealing useful altitude-resolved ionospheric responses to solar eclipses (Goncharenko et al., 2018; MacPherson et al., 2000; Salah et al., 1986). Recently, leveraging the expanding availability of diverse ground-based and space-based ionospheric measurements, pioneering efforts have been undertaken to reconstruct the 3-D ionospheric structure during eclipses using tomography and data assimilation techniques (Aa et al., 2023; Aa, Coster, et al., 2024; C. H. Chen et al., 2022; He et al., 2018; Lin et al., 2023; Zhai et al., 2023).
2. How does the topside ionospheric electron density behavior differ from that of the bottomside ionosphere during an eclipse? The anticipated variation in the topside ionosphere during a solar eclipse can be highly intricate, owing to the contrasting influences of the photo-chemical processes and the plasma diffusion above the F2 peak. This makes the topside ionosphere a key region to better understand eclipse's effects. Nevertheless, the availability of data on the topside ionosphere remains an important issue. For example, while ionosondes can offer valuable observations, particularly in the F2 peak region, they lack direct measurements of the topside ionosphere. In situ measurements from satellites can provide crucial topside information (Maji et al., 2017; Perry et al., 2019; Yau et al., 2018). Considering the transient nature of a solar eclipse, however, these measurements are far from adequate due to the limited number of samples along narrow swathes of satellite orbits at fixed altitudes. Therefore, better characterizing the topside ionospheric behavior and analyzing its difference from the bottomside ionosphere during a solar eclipse is still an important issue.

On 08 April 2024, a total solar eclipse traversed across North America from Mexico to Canada, crossing the continental United States during ~17–21 UT with a dense network of observational equipment in place. Similar to that of 2017, this Great American solar eclipse presents another valuable opportunity for analyzing ionospheric effects. In this paper, we employ multi-instrument observations and a 3-D regional data assimilation system to collectively investigate time-evolving 3-D ionospheric electron density variations during this eclipse. The observations encompass data from the Millstone Hill incoherent scatter radar, ionosonde measurements, and Swarm satellite in situ measurements. The data assimilation system is a TEC-based ionospheric data assimilation system (TIDAS, Aa et al. (2022)) that employs the Naval Research Laboratory (NRL) SAMI3 (Huba & Krall, 2013; Huba et al., 2000) as the background model, which can reconstruct high-fidelity 3-D time-evolving Ne distribution over the continental US and adjacent areas. By combining observations and data assimilation, our goal is to analyze the altitude-dependent 3-D ionospheric variations during the eclipse to further address aforementioned questions.

2. Data Sets, Model, and Methodology

The Millstone Hill incoherent scatter radar, operated by the Massachusetts Institute of Technology since 1960, is a powerful ultra-high frequency radar system that utilizes the Thomson scatter remote sensing method to measure the midlatitude and subauroral ionosphere in the North American sector. The radar system consists of a fully steerable antenna with a diameter of 46 m and a fixed-zenith antenna with a diameter of 68 m, capable of measuring ionospheric parameters (e.g., plasma density, velocity, temperature) within a range of 100–1,000 km with complete altitudinal profiles (Erickson et al., 2011; Foster & Vo, 2002). In this study, we will show the azimuth scan results from the steerable antenna with wide coverage at $6°$ elevation to demonstrate the 3-D variations in electron density over the continental US during the eclipse. Moreover, we will analyze ionospheric peak parameters and electron density profiles measured at four ionosondes: Austin (30.4°N, 97.7°W), Boulder (40.0°N, 105.3°W), Alpena (45.1°N, 83.6°W), and Wallops Island (37.9°, 75.5°). The ionospheric peak parameters were given by automatically scaled digisonde and then manually calibrated. The temporal resolution is 5 min for Austin, Boulder, and Wallops and 7.5 min for Alpena. Additionally, we will analyze in situ electron density measurements from the Langmuir probe onboard the Swarm satellites in the topside ionosphere. In particular, the Swarm-B satellite, orbiting at approximately 520 km altitude, fortuitously passed through the central shadow region during the eclipse hours.

The SAMI3 (Sami3 is Also a Model of the Ionosphere) is a physics-based global three-dimensional model of the ionosphere/plasmasphere system, built upon the foundation of SAMI2 (Huba & Krall, 2013; Huba et al., 2000). SAMI3 simulates the plasma and chemical evolution of seven ion species (H^+, He^+, N^+, O^+, NO^+, N_2^+, and O_2^+). The temperature equation is solved for electrons and for three ion species (H^+, He^+, and O^+). Ion inertia is incorporated in the ion momentum equation for deriving motion along the geomagnetic field lines and calculating drifts transverse to the field lines. For more details about SAMI3 model, readers may refer to Huba et al. (2017). SAMI3 uses empirical models (e.g., NRLMISISE00 and HWM14) to specific initial conditions, which also assumes quiet time conditions and neglect the high-latitude convection potential because the eclipse mainly occurs at low-to-mid latitudes. In this study, the solar and geomagnetic parameters utilized in SAMI3 are set to be F10.7 = 128 solar flux unit (sfu, 1 sfu = 10^{-22} W/m^2/Hz) and Ap = 4, which agree well with the realistic conditions. SAMI3 simulation is conducted with the solar EUV radiation being appropriately obscured during the eclipse period. Minor gradients in solar EUV were not considered in the mask, which can be due to active regions that are not blocked, gradients in coronal emission and line-of sight geometry (Mrak, Semeter, Drob, & Huba, 2018). The obscuration factors at given time and location during the eclipse are calculated using the Naval Observatory Vector Astrometry Software (Kaplan et al., 2012). For more details about the obscuration equation, readers may refer to Huba and Drob (2017). SAMI3 output of electron density over continental US and adjacent areas serves as the initial background state for implementing subsequent data assimilation processes.

TIDAS is a new TEC-based ionospheric data assimilation system covering the continental US and adjacent regions (20°–60°N, 60°–130°W, and 100–800 km), which utilizes a hybrid Ensemble-Variational algorithm to assimilate a diverse range of ionospheric TEC/Ne measurements obtained from ground-based and space-based sources, including the line-of-sight TEC data from 2,000+ ground-based GNSS receivers located across the North America, COSMIC-I/II radio occultation data, JASON satellite altimeter TEC data above ocean surfaces, and the Millstone Hill incoherent scatter radar data (Aa et al., 2022). For each time step, TIDAS first calculates a

non-stationary location-dependent background error covariance utilizing ensemble statistics from the background model, which has the merits of better representing the realistic ionospheric correlation with non-homogeneous expression. Subsequently, the measurement update step employs a three-dimensional variational (3DVAR) technique to minimize a cost function, which represents the weighted discrepancies between the background state and the observations, computing the maximum likelihood estimation of the state variable (i.e., electron densities) (Bust et al., 2004). TIDAS has the capability to reconstruct high-fidelity 3-D time-evolving distributions of ionospheric electron density, with a spatial-temporal resolution of $1° \times 1°$ in latitude and longitude, 20 km in altitude, and a time cadence of 5 min. This makes TIDAS a powerful tool for analyzing the altitude-resolved multi-scale midlatitude ionospheric structures. The initial success of utilizing TIDAS to reconstruct eclipse-induced ionospheric disturbances has been demonstrated for the 2017 Great American solar eclipse (Aa et al., 2023) and the 2023 annular solar eclipse (Aa, Coster, et al., 2024), respectively. We note that the default background model of TIDAS is the NeQuick-2, an empirical ionospheric electron density model known for its computational efficiency, although it typically represents the climatological rather than weather features of the ionosphere (Nava et al., 2008). Thus, to better capture the ionospheric electron density variations due to transient solar EUV obscurations during the eclipse, this study uses the aforementioned SAMI3 Ne outputs as the initial background model of TIDAS for data assimilation. Subsequently, the 3DVAR technique is used to assimilate realistic observations. The temporal update of the state variable is implemented through using a linear prediction model as demonstrated in Aa, Zhang, et al. (2024). Furthermore, the known sources of error came from the error propagation from the input to the output and inverse problems that result from the calibration of background model against measurements. For the majority of data sets such as the line-of-sight TEC and incoherent scatter radar data, observed uncertainties were used to represent the measurement error in the data assimilation. For more details about the TIDAS data assimilation technique, readers may refer to Aa et al. (2022) and Aa, Zhang, et al. (2024).

3. Results

3.1. ISR and Ionosondes Measurements

The 2024 total solar eclipse traveled across the continental US from Southern Texas to Northeast Maine during ~17–21 UT on 08 April. Figure 1 depicts the 3-D spatial distributions of ionospheric electron density alongside the corresponding 2-D horizontal projection maps at eight different UTs ranging from 17:17 UT to 20:56 UT on 08 April, measured by the steerable antenna of Millstone Hill incoherent scatter radar. As illustrated in each panel, the steerable antenna provided an extensive azimuth scan from $-43°$ to $-147°$ in 12 min among half-hour duty cycle with a 6° elevation, offering altitude-resolved electron density measurements with wide spatial coverage of ~20° in longitude and ~30° in latitude. To reduce uncertainties stemming from significant differences in range, our focus lies on analyzing the electron density variations within the F region between 200 and 400 km during the eclipse.

During 17:17–17:29 UT, Figure 1a shows that the pre-eclipse level of ionospheric F-region electron density in the central US was about $8-13 \times 10^{11}/m^{-3}$ in the vicinity of the totality path, where the radar's field-of-view has not been affected by the eclipse. Starting from 17:47 UT (Figure 1b), the eclipse gradually progressed across the radar's field-of-view, with the obscuration levels therein reaching 25%–50% during 18:16–18:28 UT (Figure 1c), 50%–75% during 18:46–18:58 UT (Figure 1d), 60%–100% during 19:16–19:27 UT (Figure 1e), and 25%–50% during 19:45–19:57 UT (Figure 1f), respectively. Correspondingly, the ionospheric F-region electron density demonstrated a significant cascading reduction across those sequential panels, reaching as low as $4-6 \times 10^{11}/m^{-3}$ near the totality path during 19:45–19:57 UT (Figure 1f). This corresponds to a 30%–55% reduction of F-region electron density compared to the pre-eclipse counterparts, which is consistent with previous studies on the depletion level of F-region peak electron density (Aa, Coster, et al., 2024; Goncharenko et al., 2018; Reinisch et al., 2018). Moreover, during the recovery phase of the eclipse from 19:45 to 20:56 UT (Figures 1f–1h), Millstone Hill ISR measurements showed that the F-region electron density remained at relatively low levels of $4-7 \times 10^{11}/m^{-3}$, implying a prolonged recovery period at this altitude that will be further analyzed using data assimilation results in next section.

Furthermore, by comparing Figures 1a and 1f, it is noteworthy that the reduction in electron density displayed an asymmetric north-south distribution with respect to the totality path: there was a relatively greater decrease in Ne toward the equatorward portion of the totality path (40%–55%) compared to the poleward region (30%–40%),
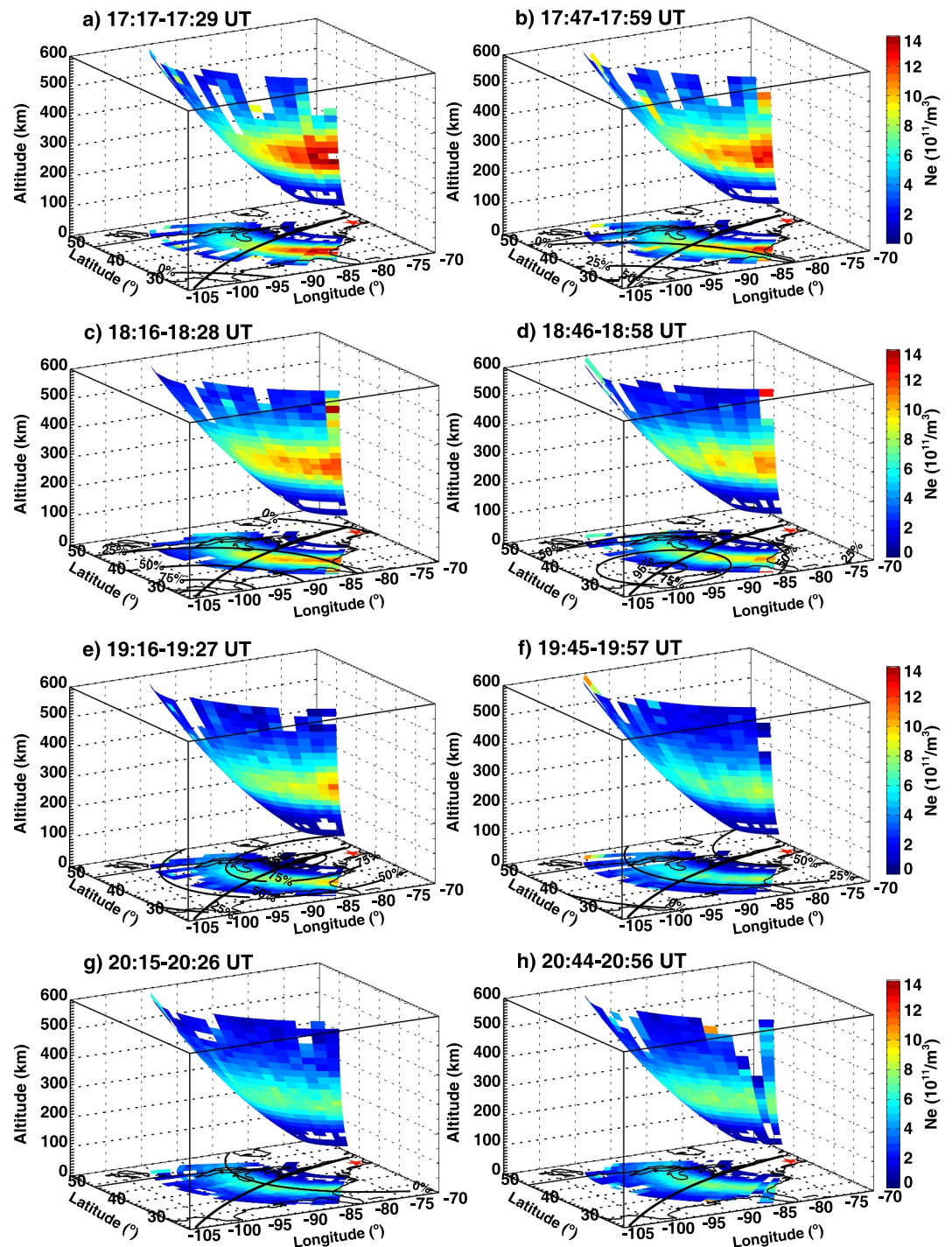
Figure 1. (a–h) 3-D spatial distributions of ionospheric electron density and the corresponding 2-D horizontal projection maps in geodetic coordinates at eight different UTs on 08 April 2024, measured by the wide-coverage azimuth scan of the steerable antenna of Millstone Hill incoherent scatter radar (red star). The totality path and the 0%, 25%, 50%, 75%, and 95% obscuration zones are included in each panel.

despite similar degrees of obscuration. This asymmetric phenomenon was previously reported for ionospheirc TEC responses during an eclipse (e.g., Aa et al., 2021; Cherniak & Zakharenkova, 2018; Huang et al., 2020), which is likely caused by the following three mechanisms: (a) Background condition and solar zenith angle effect: As deduced from the Ne map in Figure 1a, the background electron and neutral density are expected to be larger at
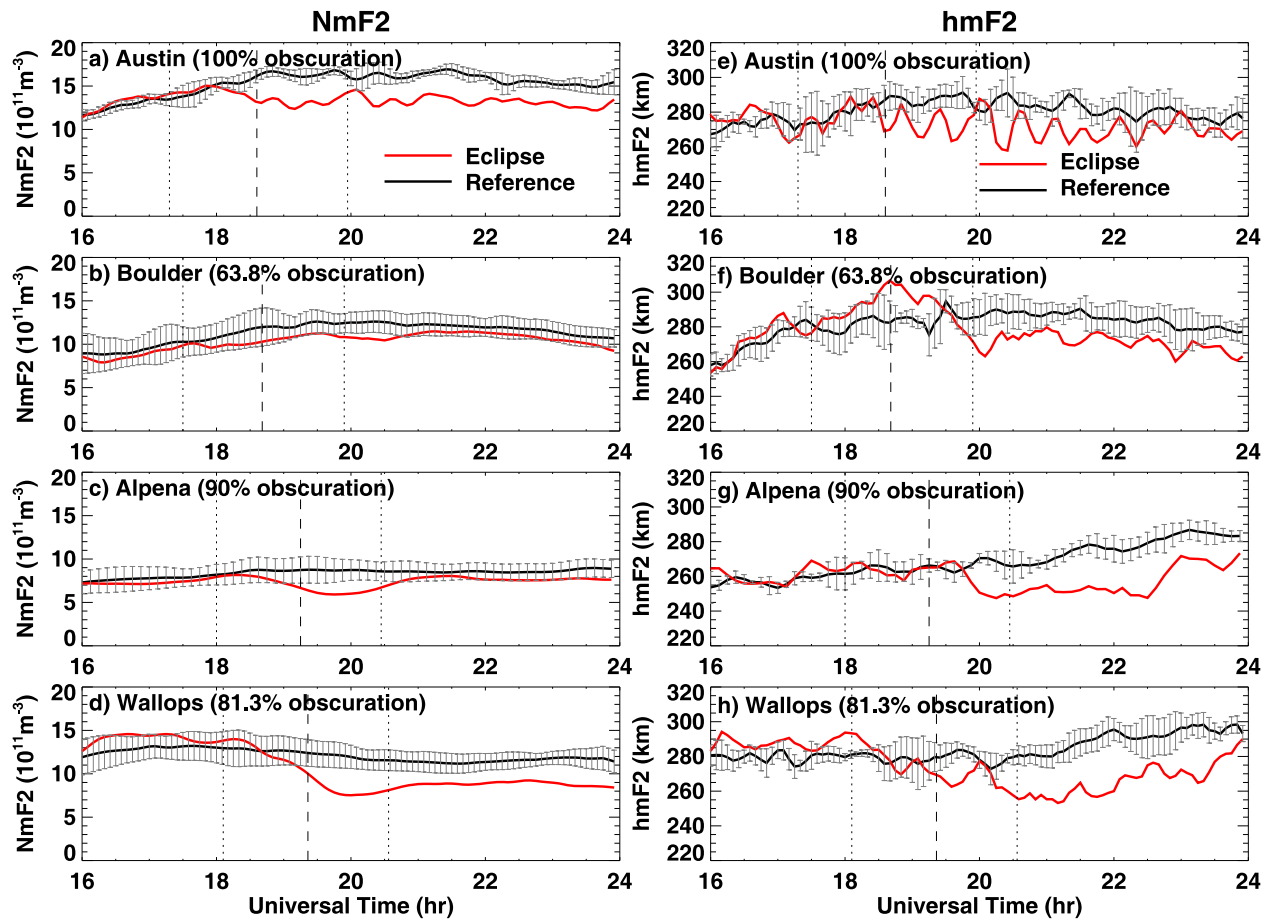
Figure 2. (a–d) F2 region peak density (NmF2) and (e–h) F2 region peak height (hmF2) measurements at four ionosondes during the eclipse and reference periods, respectively. Vertical lines denote the local eclipse start, maximum, and end times.

lower latitudes to the equatorward side of the totality path. The larger neutral concentration is associated with larger ionospheric loss coefficients, leading to a greater depletion in electron density at lower latitudes to the equatorward of the totality path (Ding et al., 2010; Le et al., 2008). Moreover, at lower latitudes, the smaller solar zenith angle would lead to a greater decrease in ion production rate due to cosine-type relationship, even when the degree of obscuration and solar EUV reduction is the same as at higher latitudes. (b) Neutral wind convergence effect: The drastic reduction in solar irradiation will cause atmospheric cooling in the eclipse zone, resulting in neutral wind convergence toward the low-pressure totality region (Müller-Wodarg et al., 1998; St.-Maurice et al., 2011; Wang et al., 2019). Thus, the neutral wind perturbation is primarily poleward (equatorward) to the equatorward (poleward) side of the totality path. At lower latitudes, the poleward wind is anticipated to drag the plasma along magnetic field lines to a lower altitude, where a higher collision and recombination rate occur, leading to a greater reduction in electron density to the south of the totality path. Similarly, the opposite trend occurs at higher latitudes on the poleward side of the totality path. (c) Dip angle and downward diffusion effect: Some simulation studies suggest that the smaller reduction in TEC at higher latitude can be attributed to the larger downward diffusion flux due to larger dip angle in this region, which partially compensates for plasma loss and mitigates the depletion of F-region electron density (e.g., Le et al., 2009).

Figure 2 shows the F2-layer peak density (NmF2) and F2-layer peak height (hmF2) during 16–24 UT on the eclipse and reference days, as measured by four ionosondes: Austin (maximum obscuration: 100%), Boulder (maximum obscuration: 63.8%), Alpena (maximum obscuration: 90.0%), and Wallops Island (maximum obscuration: 81.3%). Here, the reference values are calculated as the 3-day average from 2 days before the eclipse (6 and 7 April) and 1 day after the eclipse (9 April). All these days were under geomagnetically quiet conditions with approximately the same solar activity levels (F10.7 = 123–125 sfu) as that of the eclipse day. Due to the
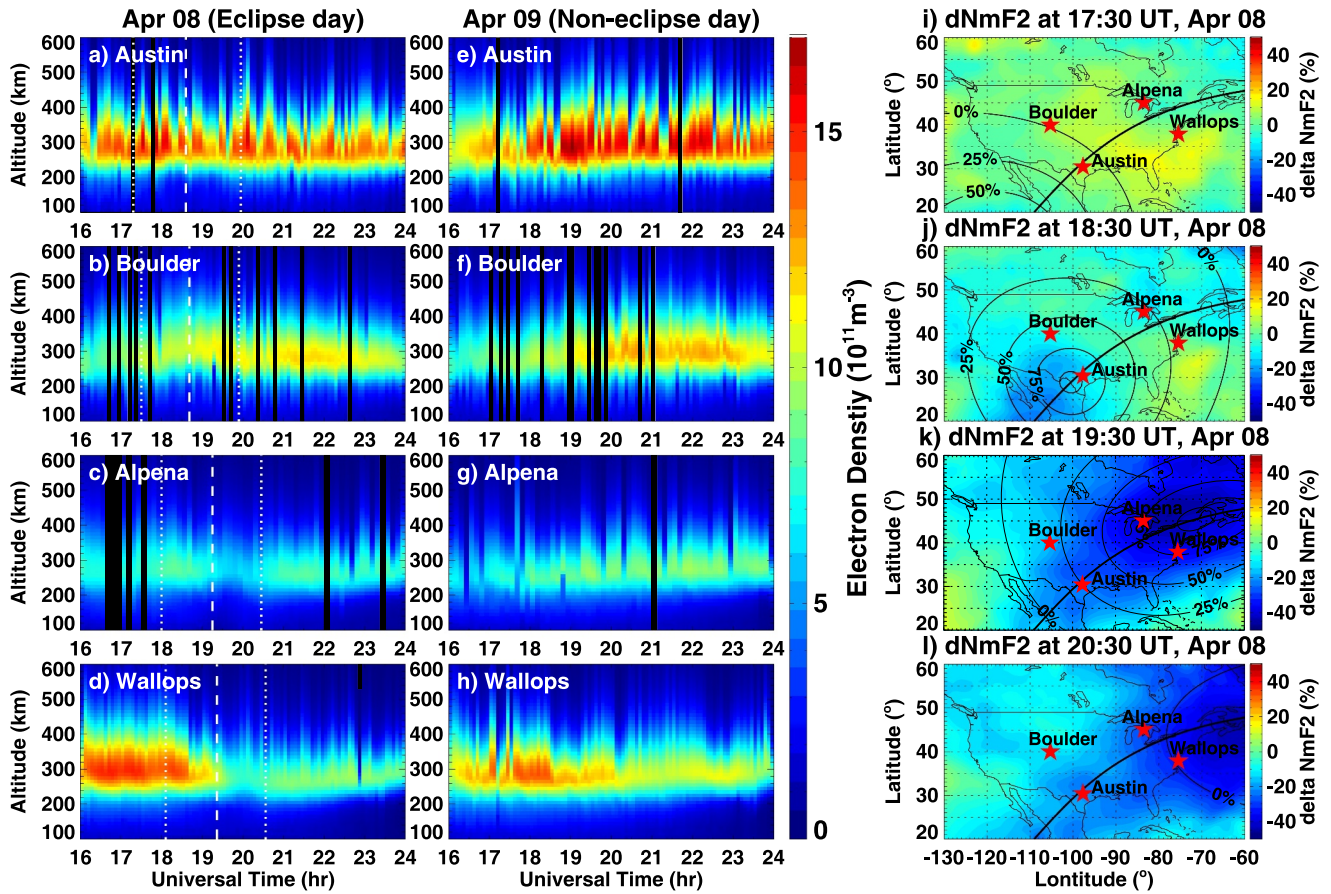
Figure 3. (a–h) Electron density profiles measured by four ionosondes between 16 and 24 UT on the day of the eclipse (08 April) and the following day (09 April), respectively. Vertical white lines denote the local start, maximum, and end times of the eclipse. (i–l) Delta NmF2 maps reconstructed using data assimilation for four UTs between 17:30 and 20:30 UT on 08 April 2024. The locations of four ionosondes are marked with stars, along with the eclipse totality path and lines indicating different obscuration zones.

suppression of photo-ionization during the eclipse, the NmF2 exhibited a noticeable reduction of 2–5×10^{11} el/m^3 at these ionosondes (Figures 2a–2d), with the maximum depletion of $\sim$26% at Austin, $\sim$20% at Boulder, $\sim$37% at Alpena, and $\sim$42% at Wallops Island. Moreover, regarding the hmF2 variation (Figures 2e–2h) during the eclipse day, there were different behaviors observed in the eclipse umbra region (i.e., Austin) compared to the penumbra region (i.e., Boulder, Alpena, and Wallops Island). In particular, at the Austin station, where the maximum obscuration is 100%, the hmF2 exhibited not only a noticeable post-eclipse reduction but also significant wavelike fluctuations, with perturbations of 10–25 km in magnitude and a period of $\sim$30 min. Such a wavelike feature of TID in the post-eclipse phase can also be observed in the NmF2 at Austin, with the fluctuation magnitudes of 1–2×10^{11} el/m^3 (5%–10%). For the other three stations located in the penumbra region, the hmF2 showed a slight enhancement of 10–20 km in the initial phase of the eclipse, followed by a prolonged reduction in peak height during the recovery phase of the eclipse that was 20–30 km lower than the reference values. Such an early enhancement and later reduction behavior of hmF2 has also been reported during the 2017 total solar eclipse (Reinisch et al., 2018) and the 2023 annular solar eclipse (Aa, Coster, et al., 2024). We will further analyze the mechanisms behind these ascending, descending, and wavelike fluctuations of the peak height in the discussion section.

Figures 3a–3d and 3e–3h display the ionosonde electron density profiles between 16 and 24 UT on the eclipse day and the following day, respectively. Due to the eclipse-induced reduction in photo-ionization, the common response at all these ionosondes is a clear electron density bite-out during the eclipse period, particularly distinct after the local maximum obscuration in the F-region between 200 and 400 km. However, it is worth noting that these Ne profiles are derived from automatic ionosonde measurements, which contain sporadic data gaps and
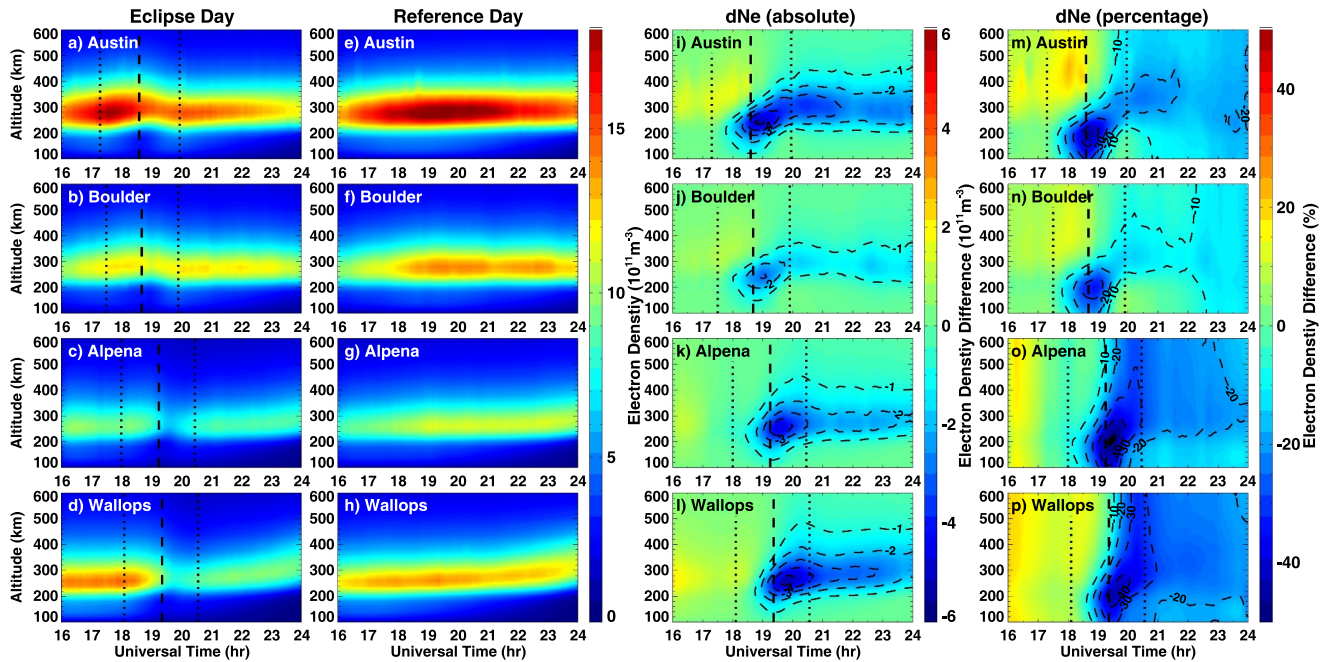
Figure 4. (a–h) Electron density profiles reconstructed by SAMI3-TIDAS data assimilation at the locations of the four ionosondes between 16 and 24 UT on the eclipse day (8 April) and the reference day (mean of 6, 7, and 9 April), respectively. (i–p) The absolute delta Ne and percentage delta Ne between the eclipse day and reference day. Vertical lines denote the local start, maximum, and end times of the eclipse.

some large errors. Moreover, the topside Ne profile above the F2-region peak height was not obtained through realistic measurements but derived based on an α-Chapman assumption of the plasma distribution (Reinisch & Huang, 2001). Therefore, these ionosonde results are utilized to offer a preliminary and qualitative estimation of the eclipse's impact. A detailed examination of the 3-D ionospheric electron density variations will be conducted using the data assimilation approach in the following section.

3.2. Data Assimilation Results

Figures 3i–3l show delta NmF2 maps reconstructed using SAMI3-TIDAS data assimilation over the continental US at four UTs between 17:30 and 20:30 UT on 08 April 2024. The locations of four ionosondes are marked with stars, along with the eclipse totality path and lines indicating different obscuration zones. At 17:30 UT (Figure 3i), the penumbral shadow of the eclipse had just entered the North American region from the Gulf of California, and the continental US showed some slight dNmF2 fluctuations within ±5%. At 18:30 UT (Figure 3j), the eclipse umbra reached the Southwest US border, and the dNmF2 showed a 10%–20% decrease in the trailing area of the eclipse within the 50% obscuration zone over Texas and northern Mexico. At 19:30 UT (Figure 3k), the totality had swept across the continental US and reached the New England area in the northeast US. The dNmF2 showed a substantial depletion of 25%–45% in the vicinity of the totality path, with the most notable depletion occurring in the eclipse trailing region within 75%–95% obscuration zone. Additionally, in the post-eclipse phase at 20:30 UT (Figure 3l), the majority of continental US registered a 10%–30% reduction in dNmF2, while there was still some 40% depletion around the maritime provinces of Canada (i.e., New Brunswick, Nova Scotia, and Prince Edward Island) where the eclipse had not yet finished.

Figures 4a–4d and 4e–4h display the temporal variation of electron density profiles reconstructed using data assimilation at the locations of the four ionosondes on the eclipse day and the reference day, respectively. As can be seen, the data assimilation results managed to reproduce the altitude-resolved electron density bite-out phenomenon during the eclipse, exhibiting a consistent trend with that of ionosonde data sets. To better examine the eclipse-induced ionospheric response, Figures 4i–4l and 4m–4p show the absolute delta Ne and percentage delta Ne profiles between eclipse and reference values at corresponding ionosondes locations, respectively. A noticeable feature in all these profiles is a significant reduction in Ne of $2–5 \times 10^{11}$ el/m^3 (~20%–50%) during the eclipse period, with the maximum depletion occurring in the ionospheric F region between 200 and 250 km about

10–20 min after the local maximum obscuration. Specifically, the maximum electron density reduction is about 47.3% at 200 km over Austin, 33.9% at 200 km over Boulder, 51.4% at 220 km over Alpena, and 46.2% at 220 km over Wallops Island. This percentage level of reduction in electron density is similar to that observed during the 2017 Great American total solar eclipse (Aa et al., 2023; Goncharenko et al., 2018; Reinisch et al., 2018), although the solar activity level for the 2024 total solar eclipse (F10.7 index = 125 sfu) is much higher than that in 2017 (F10.7 index = 89 sfu). However, the absolute reduction in Ne for this solar eclipse is 3–4 times larger than those at lower solar activity years, which indicates the effect of solar activity level on depletion levels. Additionally, the reanalyzed electron density reduction around the F2 region peak height (260–300 km) exhibits good agreements with the reduction level in NmF2 shown in Figure 2, indicating the reliability and accuracy of data assimilation results. Moreover, the reduction in electron density during the eclipse exhibited a significant altitude-dependent time-delay feature, wherein the response time gradually delayed with respect to increasing altitude. Specifically, the Ne in the lower altitudes (E region and bottomside F region) demonstrated a much quicker response, occurring 1–2 hr earlier than that in the higher altitudes (F2 region and the topside ionosphere). For instance, at the Austin station (Figures 4i and 4m) where the maximum obscuration was 100%, the electron density at E-F1 region (100–200 km) showed an immediate decrease after the onset of the local eclipse, reaching a 10% depletion at 17:40 UT. In contrast, the electron density around the F2 peak region (~300 km) exhibited a comparatively slower response, reaching the same 10% depletion with a 1-hr delay at 18:40 UT. Additionally, the electron density response in the topside ionosphere (400–600 km) experienced further delay achieving the same 10% depletion at 19:40 UT, which was one hour later compared to that observed in the F2 peak region and two hours later compared to that in the E-F1 region. A similar altitude-dependent response in Ne reduction was also evident at other ionosonde locations (i.e., Boulder, Alpena, and Wallops Island). Likewise, the recovery phase of electron density also exhibited a noticeable altitude-dependent feature, showcasing significant discrepancies between the bottomside and topside ionosphere. In particular, the ionospheric E-F1 region demonstrated a relatively quick recovery in electron density after the local maximum obscuration, as can be seen in Figures 4i–4l. In contrast, the electron density in the F2 region and topside ionosphere underwent a much slower recovery pace, sustaining a prolonged depletion of $1.5–2.5 \times 10^{11}$ el/m^3 (~10%–20%) even 3–4 hr after the end of local eclipse through local evening.

To further investigate the aforementioned altitude-dependent time delay of electron density variations across the bottomside and topside ionosphere, Figure 5a shows eight individual dNe profiles during the eclipse period between 17:00 and 20:30 UT with 30 min intervals. These profiles are derived by SAMI3-TIDAS data assimilation from a lower-latitude location (24°N, 105°W) in the totality path, where the eclipse occurred in the local morning. By comparing the profiles at 17:00 UT (black) and 17:30 UT (purple), it is evident that the bottomside ionospheric Ne exhibited an immediate reduction of ~20% shortly after the beginning of the eclipse, while the topside ionosphere maintained essentially unchanged. At 18:00 UT (cyan) and 18:30 UT (yellow), when the local obscuration was around maximum of nearly 100%, the reduction in Ne at the bottomside ionosphere further intensified to 35%–50%, with the maximum depletion occurring around 200 km. In contrast, the ionospheric Ne above 300 km did not exhibit clear reduction but rather showed a slight enhancement in the waxing phase of the eclipse, likely related to the initial layer uplift to a higher altitude (shown in Figure 2) with slower recombination rate. Additionally, starting from 18:30 UT, there was a rapid rebound in the bottomside ionospheric Ne during the eclipse waning phase, which quickly recovered to less than 10% reduction in an hour. Meanwhile, the electron density in the F2 region and topside ionosphere began to noticeably decrease following the local maximum obscuration, reaching a peak reduction of ~20% between 19:30 and 20:30 UT, by which time the bottomside ionospheric Ne had already recovered. We will further explore the potential mechanisms of such an altitude-dependent characteristic in the discussion section. To quantify the time delay of Ne response between the bottomside and topside ionosphere, Figure 5b shows the corresponding temporal variation of dNe at different altitudes from 100 to 700 km, with the dots representing the maximum depletion at each altitude. As observed, the maximum Ne depletion occurred after the local maximum obscuration with a time delay at different altitudes, which is listed in Table 1. Specifically, there was a slight time delay of 5–10 min at 100 and 200 km, a modest delay of 30 min at 300 km, a longer delay of 100 min at 400 and 500 km, and a prolonged delay of 145 min at 600 and 700 km. One notable point is that the maximum depletion at altitudes of 400 km and above occurred even after the local eclipse had ended, by which time the bottomside ionospheric Ne between 100 and 200 km had already recovered to pre-eclipse levels. Likewise, Figures 5c and 5d show individual dNe profiles and corresponding temporal variations at a mid-latitude location (44°N, 75°W) in the totality path, where the eclipse occurred in the
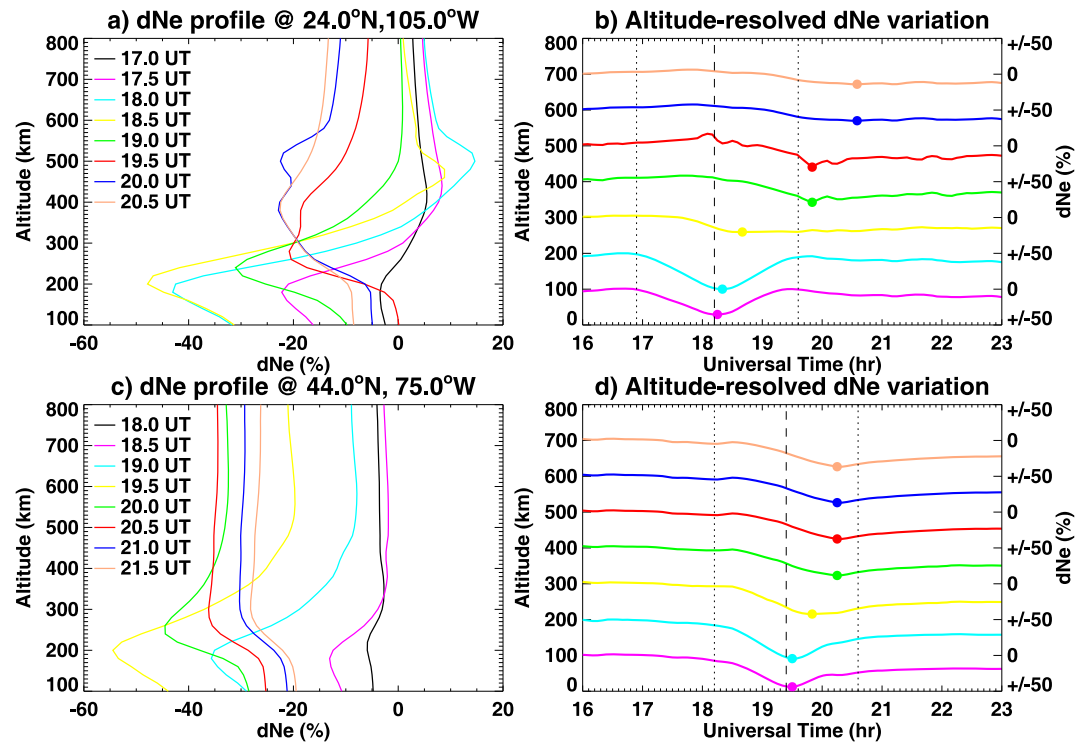
Figure 5. (a and c) dNe profiles reconstructed by SAMI3-TIDAS data assimilation across eight UTs with 30-min interval at two locations in the totality path. (b and d) The corresponding temporal variation of dNe at different altitudes. The dots represent the maximum Ne depletion at each height. Vertical lines denote the local start, maximum, and end times of the eclipse.

local afternoon. As observed, the bottomside ionospheric Ne between 100 and 200 km experienced an immediate reduction after the onset of the local eclipse, reaching a maximum depletion of 45%–55% around 5 min after the local maximum obscuration. The ionospheric Ne reduction around the F2 peak region (~300 km) exhibited a moderate lag, reaching a maximum depletion of ~40% about 30 min after the local maximum obscuration. The ionospheric Ne reduction at 400 km and above was even more delayed, reaching a maximum depletion of 25%–35% about 55 min after the local maximum obscuration. In short, the time delay between the bottomside and topside ionospheric Ne response was ~50 min, which was smaller than that at the lower-latitude location (~140 min) as shown in Figures 5a and 5b. This suggests that the altitude-dependent ionospheric response is likely also impacted by latitudinal and local time difference, which will be further analyzed in the discussion section.

To get a comprehensive view of the time-evolving altitude-dependent ionospheric electron density response during the eclipse, Figure 6 displays the horizontal maps of delta Ne reconstructed using data assimilation at different altitudes ranging from 200 to 600 km for four UTs between 17:30 and 20:30 UT on 08 April 2024. These

Table 1
Time Delay Between the Maximum Ne Depletion and Maximum Obscuration at Different Altitudes

	Lower-latitude location (24°N, 105°W)	Midlatitude location (44°N, 75°W)
100 km	5 min	5 min
200 km	10 min	5 min
300 km	30 min	30 min
400 km	100 min	55 min
500 km	100 min	55 min
600 km	145 min	55 min
700 km	145 min	55 min
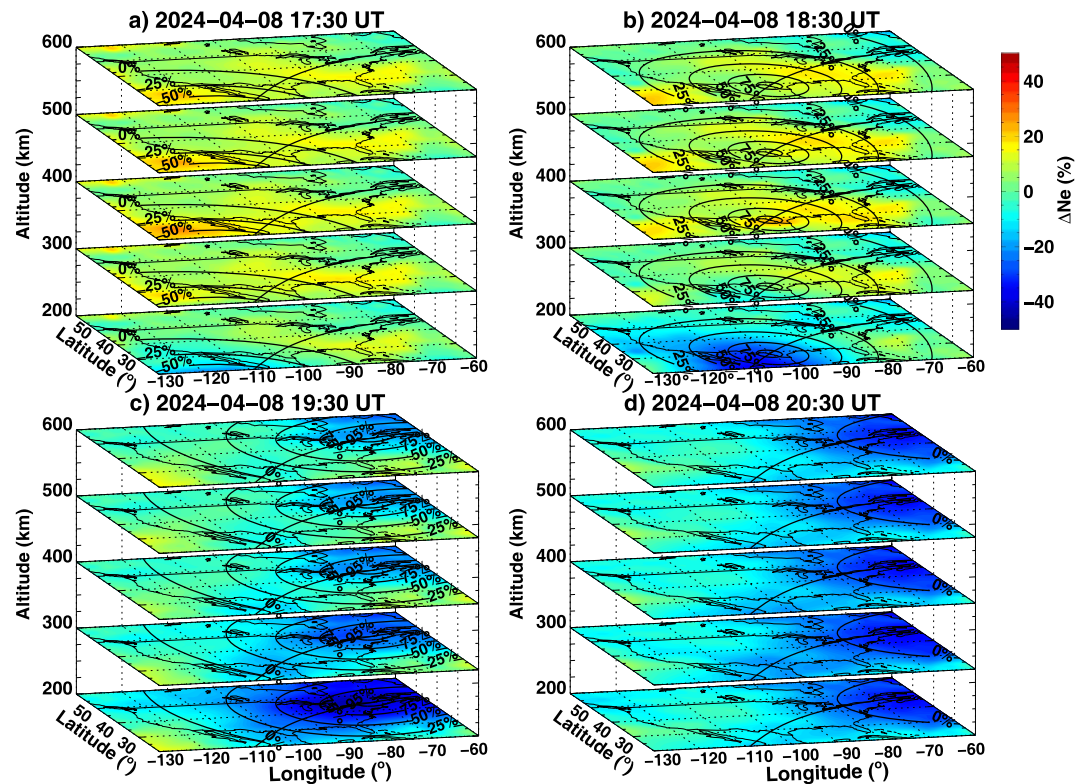
Figure 6. (a–d) 3-D distribution of the delta Ne maps at different altitudes, reconstructed using data assimilation for four UTs between 17:30 and 20:30 UT on 08 April 2024. The path of the eclipse totality and different obscuration zones are also indicated.

panels clearly demonstrate the spatial-temporal movement of the electron density depletion across the continental US following the passage of the eclipse, with noticeable discrepancies in magnitude and time delays between the bottomside and topside ionosphere. Specifically, at 17:30 UT (Figure 6a), when the penumbral shadow had just entered the continental United States, a 10% reduction in electron density was observed at 200 km around 120°W, while no significant decrease in electron density was noted at 300 km and higher altitudes. At 18:30 UT (Figure 6b), when the eclipse shadow had extended to cover the entire continental U.S., a noticeable reduction in electron density (Ne) of 20%–40% was observed at an altitude of 200 km, around 100°—120°W near the region of totality. However, the Ne reduction around the same region at 300 km was much smaller, approximately 10%, and no clear decrease in electron density was observed at 400 km and above. At 19:30 UT (Figure 6c), within the 50% obscuration zone, the reduction in electron density was approximately 40%–50% at 200 km, 30%–40% at 300 km, and 20%–30% at 400 km and above. At 20:30 UT (Figure 6d), within the residual obscuration zone, the reduction in electron density had recovered to 20% at 200 km but remained considerably depleted ranging between 30% and 40% at 300 km and higher altitudes.

We next proceed to validate the data assimilation results in the topside ionosphere using Swarm measurements. Figure 7a shows the horizontal Ne map at 520 km overlaid with the Swarm-B satellite orbit at 19:10 UT on 08 April 2024. Figures 7b and 7c display the corresponding latitude profiles of Swarm-B in situ Ne during the eclipse and reference days, as well as the latitudinal profiles of dNe variation given by Swarm-B and data assimilation, respectively. Around 19:10 UT, Swarm-B was flying along 86°W longitude, mainly covering the 50%–100% obscuration region over continental US. The electron density reduction along Swarm path was about $0.3-1 \times 10^{11}$ el/m^3 compared with reference values. In comparison, the data assimilation results agree generally well with the Swarm in situ results, effectively reproducing the eclipse-induced Ne reduction with a consistent trend of latitudinal variation, albeit there were some small deviations of 10%–15% in magnitude. This demonstrates the reliability of data assimilation in reconstructing the topside ionospheric electron density. Moreover, Figures 7d–7f display electron density map at 520 km and latitudinal profiles similar to those of Figures 7a–7c, but for the
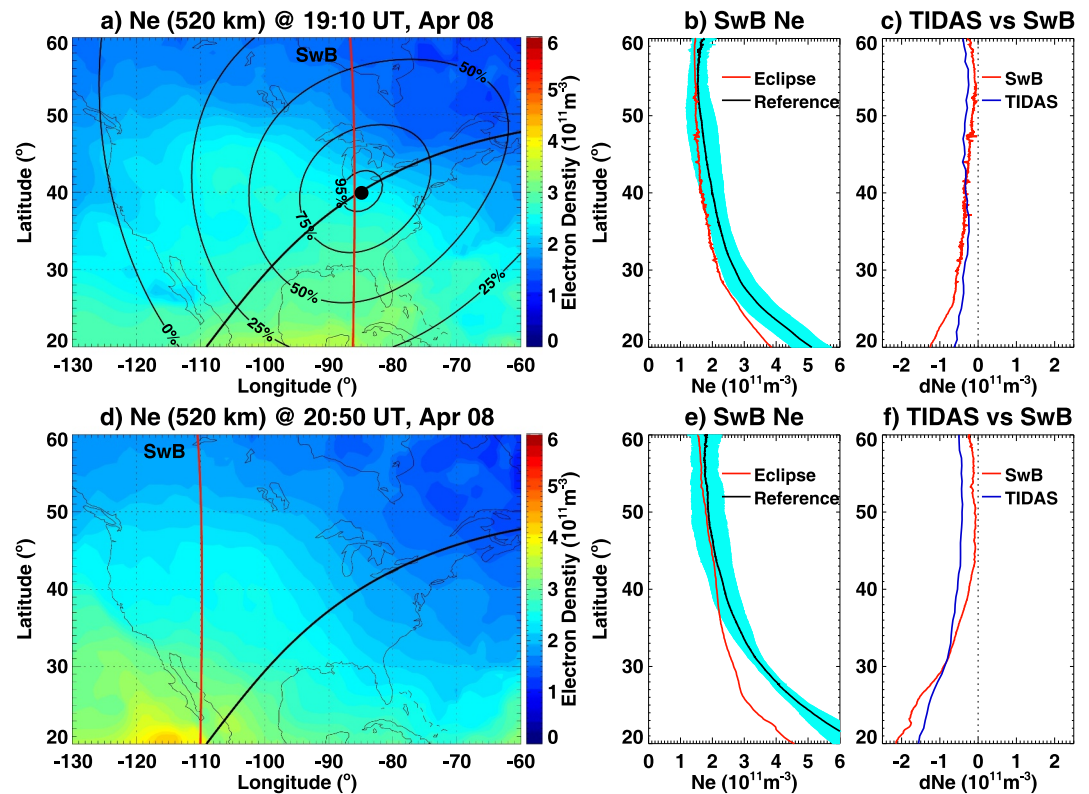
Figure 7. (a) Electron density map reconstructed using data assimilation at 520 km along with the Swarm-B satellite path (red line) at 19:10 UT on 08 April 2024. The eclipse totality path and different obscuration zones are also indicated. (b) Corresponding latitudinal profiles of Swarm-B in situ Ne. (c) Latitudinal profiles of dNe variation given by Swarm-B (red) and TEC-based ionospheric data assimilation system data assimilation (blue). Panels (d–f) are the same as (a–c), but for 20:50 UT on 08 April 2024.

subsequent pass of Swarm-B around 20:50 UT. Around this time, Swarm-B was flying along 110°W longitude in the post-eclipse phase, approximately 1.5 hr after the local eclipse had ended. Figures 7e and 7f show that the post-eclipse electron density reduction was about $0.4–2 \times 10^{11}$ el/m^3, which is more severe than that observed under substantial obscuration during the previous orbit, especially in the lower-latitude region below 35°N. Thus, the Swarm measurements also suggest that the topside ionospheric electron density tends to exhibit a much slower response compared to that in the bottomside ionosphere, reaching a more severe reduction in Ne around the ending time rather than the peak time of local obscuration. This phenomenon is consistent with the data assimilation results as shown in Figures 4–6.

4. Discussion

The ionospheric hmF2 variation exhibited a slight enhancement in the beginning phase of the eclipse, followed by a pronounced reduction of 20–30 km during the recovery phase. Several studies have indicated that the early rise of hmF2 is associated with the rapidly vanishing of electron density in the bottomside ionosphere due to the photo-chemical process, leading to the uplift of the F region peak height in ionosonde measurements (Dear et al., 2020; Lin et al., 2023; Reinisch et al., 2018; Tian et al., 2022). Our data assimilation results clearly demonstrate that the E and F1 regions experienced an immediate reduction that was much faster than that observed in the F2 region and topside ionosphere. Conversely, the data assimilation results also show that the decrease in hmF2 after the maximum obscuration can be attributed to the comparatively rapid recovery and rebuilding of the ionosphere from lower altitudes, while the F-region peak height was still experiencing significant depletion (Aa, Coster, et al., 2024).

Besides the post-eclipse reduction, the hmF2 over the umbra region displayed significant wavelike fluctuations, characterized by perturbations of 10–25 km in magnitude and a period of approximately 30 min. These mid-scale

TIDs could be a manifestation of eclipse-generated secondary gravity waves within the ionosphere-thermosphere system. Several studies have observed the ionospheric signatures of the bow-shaped gravity waves (Sun et al., 2018; Zhang et al., 2017). The upward propagation of these primary waves could grow exponentially in amplitudes before they broke at certain altitudes in the theremosphere-ionosphere, from which the energy and momentum release could generate secondary gravity waves and TIDS (Vadas & Liu, 2009), similar to that observed in prior studies (Chimonas, 1970; Harding et al., 2018; Nayak & Yiğit, 2018). However, weak signs of wavelike behavior can also be seen for the baseline with some different temporal and spatial periods, although the wavelike features were more significant on the eclipse day with dominant periodicity of ∼30 min Nayak and Yiğit (2018) observed distinct gravity wave-like signatures with wave periods around 20–90 min in the GPS TEC observation during 2017 solar eclipse, with dominant peak at 30 min wave period. This periodicity agrees well with our observations. Besides the solar eclipse, there could be also some effects from other localized wave sources, such as the thunderstorms activity near the Texas area on 08–09 April. This might potentially explain that similar wave-like features were not seen in other ionosonde locations over the penumbra region even with 90% obscuration at Alpena. Moreover, the Kp indices reached 3- a couple hours before the eclipse, so the possibility cannot be ruled out that part of the TIDs might be related to geomagnetic disturbances. Therefore, some parts of the wavelike fluctuations were likely related to non-eclipse sources such as thunderstorm/tropospheric weather and/or geomagnetic disturbances. The underlying mechanism of this post-eclipse TID needs further examination through thermospheric-ionospheric numerical simulations with additional data sets in the future.

Furthermore, the ionospheric electron density variation during the eclipse exhibited a distinct altitude-dependent feature, wherein the response time gradually delayed with respect to increasing altitude, showing different behaviors between the bottomside and topside ionosphere. In particular, the bottomside ionospheric electron density between 100 and 200 km demonstrated an immediate reduction after the onset of local eclipse, reaching maximum depletion in 5–10 min after the maximum obscuration, followed by a comparatively quick recovery. It is known that the eclipse-induced sudden changes in solar EUV and photo-ionization rate can have a more immediate impact on the photo-chemical equilibrium at lower altitudes, especially the E and F1 region (Rishbeth, 1968). This leads to the relatively instant reduction and quick recovery of electron density in the bottomside ionosphere. Furthermore, Wang et al. (2019) suggests that the combination of low temperature and convergence of disturbance winds in the shadow region leads to a local enhancement of O/N_2 shortly after the local maximum obscuration, which also significantly contributes to the electron density recovery below the F2 peak.

In contrast to the bottomside ionosphere, the topside ionospheric electron density exhibited a significantly delayed response during the eclipse, reaching maximum depletion 1–2.5 hr after the peak obscuration, even nearing the local eclipse ending. Such an extended time delay in the topside ionosphere can be attributed to the balancing effect of downward plasma diffusion. The eclipse-induced decrease in plasma temperature and pressure led to a reduction in the plasma equilibrium scale height, which resulted in an enhanced downward plasma diffusion in the F2 and topside ionosphere (e.g., Evans, 1965; MacPherson et al., 2000). The simulation result given by Wang et al. (2019) indicates that the diffusion effect is positive above the F2 peak near the maximum obscuration, which can drive substantial plasma into the shadow region in the topside ionosphere. Hence, this diffusion process can offset the net decrease in electron density caused by the photochemical effect, thereby contributing to the prolonged delay of the peak depletion timing observed in the topside ionosphere.

In the previous studies, ionospheric responses to a solar eclipse were largely analyzed using GNSS TEC observations, which showed that the eclipse-induced TEC decrease had minimum with 15–30 min lag after the maximum eclipse obscuration (Cherniak & Zakharenkova, 2018; Coster et al., 2017). However, TEC is an integrated quantity, and essential information about ionospheric altitudinal structures is absent in 2-D TEC maps. Our data assimilation study shows that the electron density reduction exhibited an altitude-dependent time delay, from 5 to 10 min in the bottomside ionosphere to 1–2.5 hr in the topside ionosphere. The aforementioned time-delay in TEC result is similar to that in the F2 peak height. These findings shed new lights that an eclipse can induce significant and complex variations in the vertical domain of the ionosphere.

Last but not least, Figure 5 and Table 1 show that the altitude-dependent feature of time delay is more pronounced at lower latitudes compared to mid-latitudes. This phenomenon might be related to the following two reasons. (a) Dip angle effect: The field-aligned diffusion has less (more) downward component in the lower-latitude (mid-latitude region) region due to smaller (larger) magnetic dip angle (Le et al., 2009). Thus, it would be more difficult for the diffusion process to compensate for the eclipse-induced electron density depletion and smooth out the

altitudinal discrepancies in lower-latitude locations. (b) Local time effect: In the lower-latitude location within the totality path, the eclipse commenced during the local morning when the photo-chemical processes would play a more dominant role in ionospheric formation compared to transport processes (Rishbeth et al., 1995). Thus, the ambipolar diffusion would take a longer time to counteract the net reduction in electron density due to the predominant photo-chemical effect. In comparison, the eclipse took place in the local afternoon at midlaititude location within the totality path, by which time the photo-chemical and transport processes had established a balanced relationship. Therefore, the decrease in electron density due to reduction in photo-ionization would be more efficiently compensated by dynamic processes.

5. Conclusions

This paper presents a multi-instrument and data assimilation study of the 3-D ionospheric electron density variations during the total solar eclipse on 08 April 2024, using Millstone Hill ISR measurements, ionosonde observations, Swarm in situ data set, and the SAMI3-TIDAS data assimilation system. The high-fidelity altitude-resolved electron density responses to the eclipse over the continental US and adjacent regions are reconstructed and analyzed. The main results are summarized as follows.

1. The ionospheric hmF2 exhibited a slight enhancement in the beginning phase of the eclipse, followed by a pronounced reduction of 20–30 km during the recovery phase. The hmF2 over the eclipse umbra region displayed significant TID characteristics after the maximum obscuration, characterized by wavelike fluctuations of 10–25 km in magnitude and a period of ∼30 min. Besides the solar eclipse, there could be also some effects from other wave sources, such as thunderstorm/tropospheric weather and/or geomagnetic disturbances.
2. The solar eclipse caused a substantial reduction in ionospheric electron density by 20%–50% near the totality path, with the maximum depletion occurring in the ionospheric F-region around 200–250 km. The electron density variation exhibited a significant altitude-dependent feature, wherein the response time gradually delayed with respect to increasing altitude.
3. The bottomside ionospheric electron density demonstrated an immediate reduction after the onset of the local eclipse, reaching maximum depletion 5–10 min after the maximum obscuration, followed by a comparatively rapid recovery. This phenomenon is related to the more immediate impact of changes in the photo-ionization rate on the photochemical equilibrium at these lower altitudes.
4. In contrast to the bottomside ionosphere, the topside ionospheric electron density exhibited a significantly delayed response during the eclipse, reaching maximum depletion 1–2.5 hr after the peak obscuration, with a more pronounced time delay at lower latitudes. This phenomenon can be attributed to the balancing effect of the plasma diffusion process, which counteracts and delays the net variation in electron density caused by the photochemical process.

Data Availability Statement

GNSS TEC data products are provided through the Madrigal distributed data system by MIT Haystack Observatory (http://cedar.openmadrigal.org/). The ionosonde data are provided by the University of Massachusetts Lowell DIDB database of Global Ionospheric Radio Observatory (https://giro.uml.edu/didbase/scaled.php). Swarm data are provided by European Space Agency (https://swarm-diss.eo.esa.int/).

References

Aa, E., Coster, A. J., Zhang, S.-R., Vierinen, J., Erickson, P. J. P. G. L., & Rideout, W. (2024a). 2-D total electron content and 3-D ionospheric electron density variations during the 14 October 2023 annular solar eclipse. *Journal of Geophysical Research: Space Physics*, *129*(3), e2024JA032447. https://doi.org/10.1029/2024JA032447

Aa, E., Zhang, S.-R., Erickson, P. J., Goncharenko, L. P., Coster, A. J., Jonah, O. F., et al. (2020). Coordinated ground-based and space-borne observations of ionospheric response to the annular solar eclipse on 26 December 2019. *Journal of Geophysical Research: Space Physics*, *125*(11), e28296. https://doi.org/10.1029/2020JA028296

Aa, E., Zhang, S.-R., Erickson, P. J., Wang, W., & Coster, A. J. (2023). 3-D ionospheric electron density variations during the 2017 great American solar eclipse: A revisit. *Atmosphere*, *14*(9), 1379. https://doi.org/10.3390/atmos14091379

Aa, E., Zhang, S.-R., Erickson, P. J., Wang, W., Coster, A. J., & Rideout, W. (2022). 3-D regional ionosphere imaging and SED reconstruction with a new TEC-based Ionospheric Data Assimilation System (TIDAS). *Space Weather*, *20*(4), e2022SW003055. https://doi.org/10.1029/2022SW003055

Aa, E., Zhang, S.-R., Erickson, P. J., Wang, W., Coster, A. J., & Rideout, W. (2024b). 3-D ionospheric imaging over the South American region with a new TEC-Based Ionospheric Data Assimilation System (TIDAS-SA). *Space Weather*, *22*(2), e2023SW003792. https://doi.org/10.1029/2023SW003792

Aa, E., Zhang, S.-R., Shen, H., Liu, S., & Li, J. (2021). Local and conjugate ionospheric total electron content variation during the 21 June 2020 solar eclipse. *Advances in Space Research*, *68*(8), 3435–3454. https://doi.org/10.1016/j.asr.2021.06.015

Afraimovich, E. L., Palamartchouk, K. S., Perevalova, N. P., Chernukhov, V. V., Lukhnev, A. V., & Zalutsky, V. T. (1998). Ionospheric effects of the solar eclipse of March 9, 1997, as deduced from GPS data. *Geophysical Research Letters*, *25*(4), 465–468. https://doi.org/10.1029/98GL00186

Aryal, S., Evans, J. S., Correira, J., Burns, A. G., Wang, W., Solomon, S. C., et al. (2020). First global-scale synoptic imaging of solar eclipse effects in the thermosphere. *Journal of Geophysical Research: Space Physics*, *125*(9), e27789. https://doi.org/10.1029/2020JA027789

Aryal, S., Geddes, G., Finn, S. C., Mrak, S., Galkin, I., Cnossen, I., et al. (2019). Multispectral and multi-instrument observation of TIDs following the total solar eclipse of 21 August 2017. *Journal of Geophysical Research: Space Physics*, *124*(5), 3761–3774. https://doi.org/10.1029/2018JA026333

Bust, G. S., Garner, T. W., & Gaussiran, T. L. (2004). Ionospheric Data Assimilation Three-Dimensional (IDA3D): A global, multisensor, electron density specification algorithm. *Journal of Geophysical Research*, *109*(A11), A11312. https://doi.org/10.1029/2003JA010234

Chen, C. H., Lin, C. C. H., Lee, C. J., Liu, J. Y., & Saito, A. (2022). Ionospheric responses on the 21 August 2017 solar eclipse by using three-dimensional GNSS tomography. *Earth Planets and Space*, *74*(1), 173. https://doi.org/10.1186/s40623-022-01734-y

Chen, C.-H., Lin, C.-H. C., & Matsuo, T. (2019). Ionospheric responses to the 21 August 2017 solar eclipse by using data assimilation approach. *Progress in Earth and Planetary Science*, *6*(1), 13. https://doi.org/10.1186/s40645-019-0263-4

Chen, G., Qi, H., Ning, B., Zhao, Z., Yao, M., Deng, Z., et al. (2013). Nighttime ionospheric enhancements induced by the occurrence of an evening solar eclipse. *Journal of Geophysical Research: Space Physics*, *118*(10), 6588–6596. https://doi.org/10.1002/jgra.50551

Cherniak, I., & Zakharenkova, I. (2018). Ionospheric total electron content response to the great American solar eclipse of 21 August 2017. *Geophysical Research Letters*, *45*(3), 1199–1208. https://doi.org/10.1002/2017GL075989

Chimonas, G. (1970). Internal gravity-wave motions induced in the Earth's atmosphere by a solar eclipse. *Journal of Geophysical Research*, *75*(28), 5545–5551. https://doi.org/10.1029/JA075i028p05545

Cnossen, I., Ridley, A. J., Goncharenko, L. P., & Harding, B. J. (2019). The response of the ionosphere-thermosphere system to the 21 August 2017 solar eclipse. *Journal of Geophysical Research: Space Physics*, *124*(8), 7341–7355. https://doi.org/10.1029/2018JA026402

Coster, A. J., Goncharenko, L., Zhang, S.-R., Erickson, P. J., Rideout, W., & Vierinen, J. (2017). GNSS observations of ionospheric variations during the 21 August 2017 solar eclipse. *Geophysical Research Letters*, *44*(24), 12041–12048. https://doi.org/10.1002/2017GL075774

Dang, T., Lei, J., Wang, W., Zhang, B., Burns, A., Le, H., et al. (2018). Global responses of the coupled thermosphere and ionosphere system to the August 2017 great American solar eclipse. *Journal of Geophysical Research: Space Physics*, *123*(8), 7040–7050. https://doi.org/10.1029/2018JA025566

Dear, V., Husin, A., Anggarani, S., Harjosuwito, J., & Pradipta, R. (2020). Ionospheric effects during the total solar eclipse over Southeast Asia-Pacific on 9 March 2016: Part 1. Vertical movement of plasma layer and reduction in electron plasma density. *Journal of Geophysical Research: Space Physics*, *125*(4), e2019JA026708. https://doi.org/10.1029/2019JA026708

Ding, F., Wan, W., Ning, B., Liu, L., Le, H., Xu, G., et al. (2010). GPS TEC response to the 22 July 2009 total solar eclipse in East Asia. *Journal of Geophysical Research*, *115*(A7), A07308. https://doi.org/10.1029/2009JA015113

Eisenbeis, J., Occhipinti, G., Astafyeva, E., & Rolland, L. (2019). Short- and long-wavelength TIDs generated by the great American eclipse of 21 August 2017. *Journal of Geophysical Research: Space Physics*, *124*(11), 9486–9493. https://doi.org/10.1029/2019JA026919

Erickson, P. J., Beroz, F., & Miskin, M. Z. (2011). Statistical characterization of the American sector subauroral polarization stream using incoherent scatter radar. *Journal of Geophysical Research*, *116*(A5), A00J21. https://doi.org/10.1029/2010JA015738

Evans, J. V. (1965). On the behavior of FOF2 during solar eclipses. *Journal of Geophysical Research*, *70*(3), 733–738. https://doi.org/10.1029/JZ070i003p00733

Farges, T., Jodogne, J. C., Bamford, R., Le Roux, Y., Gauthier, F., Vila, P. M., et al. (2001). Disturbances of the western European ionosphere during the total solar eclipse of 11 August 1999 measured by a wide ionosonde and radar network. *Journal of Atmospheric and Solar-Terrestrial Physics*, *63*(9), 915–924. https://doi.org/10.1016/S1364-6826(00)00195-4

Foster, J. C., & Vo, H. B. (2002). Average characteristics and activity dependence of the subauroral polarization stream. *Journal of Geophysical Research*, *107*(A12), 1475. https://doi.org/10.1029/2002JA009409

Frissell, N. A., Katz, J. D., Gunning, S. W., Vega, J. S., Gerrard, A. J., Earle, G. D., et al. (2018). Modeling amateur radio soundings of the ionospheric response to the 2017 great American eclipse. *Geophysical Research Letters*, *45*(10), 4665–4674. https://doi.org/10.1029/2018GL077324

Gómez, D. D. (2021). Ionospheric response to the December 14, 2020 total solar eclipse in South America. *Journal of Geophysical Research: Space Physics*, *126*(7), e29537. https://doi.org/10.1029/2021JA029537

Goncharenko, L. P., Erickson, P. J., Zhang, S.-R., Galkin, I., Coster, A. J., & Jonah, O. F. (2018). Ionospheric response to the solar eclipse of 21 August 2017 in Millstone Hill (42N) observations. *Geophysical Research Letters*, *45*(10), 4601–4609. https://doi.org/10.1029/2018GL077334

Hairston, M. R., Mrak, S., Coley, W. R., Burrell, A., Holt, B., Perdue, M., et al. (2018). Topside ionospheric electron temperature observations of the 21 August 2017 eclipse by DMSP spacecraft. *Geophysical Research Letters*, *45*(15), 7242–7247. https://doi.org/10.1029/2018GL077381

Harding, B. J., Drob, D. P., Buriti, R. A., & Makela, J. J. (2018). Nightside detection of a large-scale thermospheric wave generated by a solar eclipse. *Geophysical Research Letters*, *45*(8), 3366–3373. https://doi.org/10.1002/2018GL077015

He, L., Heki, K., & Wu, L. (2018). Three-dimensional and trans-hemispheric changes in ionospheric electron density caused by the great solar eclipse in North America on 21 August 2017. *Geophysical Research Letters*, *45*(20), 10933–10940. https://doi.org/10.1029/2018GL080365

Huang, F., Li, Q., Shen, X., Xiong, C., Yan, R., Zhang, S.-R., et al. (2020). Ionospheric responses at low latitudes to the annular solar eclipse on 21 June 2020. *Journal of Geophysical Research: Space Physics*, *125*(10), e28483. https://doi.org/10.1029/2020JA028483

Huba, J. D., & Drob, D. (2017). SAMI3 prediction of the impact of the 21 August 2017 total solar eclipse on the ionosphere/plasmasphere system. *Geophysical Research Letters*, *44*(12), 5928–5935. https://doi.org/10.1002/2017GL073549

Huba, J. D., Joyce, G., & Fedder, J. A. (2000). Sami2 is Another Model of the Ionosphere (SAMI2): A new low-latitude ionosphere model. *Journal of Geophysical Research*, *105*(A10), 23035–23054. https://doi.org/10.1029/2000JA000035

Huba, J. D., & Krall, J. (2013). Modeling the plasmasphere with SAMI3. *Geophysical Research Letters*, *40*(1), 6–10. https://doi.org/10.1029/2012GL054300

Huba, J. D., Maute, A., & Crowley, G. (2017). SAMI3_ICON: Model of the ionosphere/plasmasphere system. *Space Science Reviews*, *212*(1–2), 731–742. https://doi.org/10.1007/s11214-017-0415-z

Jakowski, N., Stankov, S. M., Wilken, V., Borries, C., Altadill, D., Chum, J., et al. (2008). Ionospheric behavior over Europe during the solar eclipse of 3 October 2005. *Journal of Atmospheric and Solar-Terrestrial Physics*, *70*(6), 836–853. https://doi.org/10.1016/j.jastp.2007.02.016

Jonah, O. F., Goncharenko, L., Erickson, P. J., Zhang, S., Coster, A., Chau, J. L., et al. (2020). Anomalous behavior of the equatorial ionization anomaly during the 2 July 2019 solar eclipse. *Journal of Geophysical Research: Space Physics*, *125*(9), e27909. https://doi.org/10.1029/2020JA027909

Kaplan, G., Bartlett, J. L., Monet, A., Bangert, J., Puatua, W., Harris, W., et al. (2012). NOVAS: Naval observatory vector Astrometry software. *Astrophysics Source Code Library*.

Le, H., Liu, L., Yue, X., & Wan, W. (2008). The midlatitude F2 layer during solar eclipses: Observations and modeling. *Journal of Geophysical Research*, *113*(A8), A08309. https://doi.org/10.1029/2007JA013012

Le, H., Liu, L., Yue, X., Wan, W., & Ning, B. (2009). Latitudinal dependence of the ionospheric response to solar eclipses. *Journal of Geophysical Research*, *114*(A7), A07308. https://doi.org/10.1029/2009JA014072

Lei, J., Dang, T., Wang, W., Burns, A., Zhang, B., & Le, H. (2018). Long-lasting response of the global thermosphere and ionosphere to the 21 August 2017 solar eclipse. *Journal of Geophysical Research: Space Physics*, *123*(5), 4309–4316. https://doi.org/10.1029/2018JA025460

Lin, C. Y., Deng, Y., & Ridley, A. (2018). Atmospheric gravity waves in the ionosphere and thermosphere during the 2017 solar eclipse. *Geophysical Research Letters*, *45*(11), 5246–5252. https://doi.org/10.1029/2018GL077388

Lin, C.-Y., Liu, J.-Y., Lin, C. C.-H., & Chou, M.-Y. (2023). The ionospheric three-dimensional electron density variations induced by the 21 August 2017 total solar eclipse by using global ionospheric specification. *Remote Sensing*, *15*(15), 3887. https://doi.org/10.3390/rs15153887

Liu, J. Y., Sun, Y. Y., Kakinami, Y., Chen, C. H., Lin, C. H., & Tsai, H. F. (2011). Bow and stern waves triggered by the Moon's shadow boat. *Geophysical Research Letters*, *38*(17), L17109. https://doi.org/10.1029/2011GL048805

Liu, J.-Y., Wu, T.-Y., Sun, Y.-Y., Pedatella, N. M., Lin, C.-Y., Chang, L. C., et al. (2020). Lunar tide effects on ionospheric solar eclipse signatures: The August 21, 2017 event as an example. *Journal of Geophysical Research: Space Physics*, *125*(12), e28472. https://doi.org/10.1029/2020JA028472

MacPherson, B., González, S. A., Sulzer, M. P., Bailey, G. J., Djuth, F., & Rodriguez, P. (2000). Measurements of the topside ionosphere over Arecibo during the total solar eclipse of February 26, 1998. *Journal of Geophysical Research*, *105*(A10), 23055–23068. https://doi.org/10.1029/2000JA000145

Maji, S. K., Chakrabarti, S. K., Sanki, D., & Pal, S. (2017). Topside ionospheric effects of the annular solar eclipse of 15th January 2010 as observed by DEMETER satellite. *Journal of Atmospheric and Solar-Terrestrial Physics*, *159*, 1–6. https://doi.org/10.1016/j.jastp.2017.04.012

Mrak, S., Semeter, J., Drob, D., & Huba, J. D. (2018a). Direct EUV/X-Ray modulation of the ionosphere during the August 2017 total solar eclipse. *Geophysical Research Letters*, *45*(9), 3820–3828. https://doi.org/10.1029/2017GL076771

Mrak, S., Semeter, J., Nishimura, Y., Hirsch, M., & Sivadas, N. (2018b). Coincidental TID production by tropospheric weather during the August 2017 total solar eclipse. *Geophysical Research Letters*, *45*(20), 10903–10911. https://doi.org/10.1029/2018GL080239

Müller-Wodarg, I. C. F., Aylward, A. D., & Lockwood, M. (1998). Effects of a mid-latitude solar eclipse on the thermosphere and ionosphere—A modelling study. *Geophysical Research Letters*, *25*(20), 3787–3790. https://doi.org/10.1029/1998GL900045

Nava, B., Coïsson, P., & Radicella, S. M. (2008). A new version of the NeQuick ionosphere electron density model. *Journal of Atmospheric and Solar-Terrestrial Physics*, *70*(15), 1856–1862. https://doi.org/10.1016/j.jastp.2008.01.015

Nayak, C., & Yiğit, E. (2018). GPS-TEC observation of gravity waves generated in the ionosphere during 21 August 2017 total solar eclipse. *Journal of Geophysical Research: Space Physics*, *123*(1), 725–738. https://doi.org/10.1002/2017JA024845

Perry, G. W., Watson, C., Howarth, A. D., Themens, D. R., Foss, V., Langley, R. B., & Yau, A. W. (2019). Topside ionospheric disturbances detected using radio occultation measurements during the August 2017 solar eclipse. *Geophysical Research Letters*, *46*(13), 7069–7078. https://doi.org/10.1029/2019GL083195

Pradipta, R., Yizengaw, E., & Doherty, P. (2018). Ionospheric density irregularities, turbulence, and wave disturbances during the total solar eclipse over North America on 21 August 2017. *Geophysical Research Letters*, *45*(16), 7909–7917. https://doi.org/10.1029/2018GL079383

Reinisch, B. W., Dandenault, P. B., Galkin, I. A., Hamel, R., & Richards, P. G. (2018). Investigation of the electron density variation during the 21 August 2017 solar eclipse. *Geophysical Research Letters*, *45*(3), 1253–1261. https://doi.org/10.1002/2017GL076572

Reinisch, B. W., & Huang, X. (2001). Deducing topside profiles and total electron content from bottomside ionograms. *Advances in Space Research*, *27*(1), 23–30. https://doi.org/10.1016/S0273-1177(00)00136-8

Rishbeth, H. (1968). Solar eclipses and ionospheric theory. *Space Science Reviews*, *8*(4), 543–554. https://doi.org/10.1007/BF00175006

Rishbeth, H., Jenkins, B., & Moffett, R. J. (1995). The F-layer at sunrise. *Annales Geophysicae*, *13*(4), 367–374. https://doi.org/10.1007/s005850050172

Salah, J. E., Oliver, W. L., Foster, J. C., Holt, J. M., Emery, B. A., & Roble, R. G. (1986). Observations of the May 30, 1984, annular solar eclipse at Millstone Hill. *Journal of Geophysical Research*, *91*(A2), 1651–1660. https://doi.org/10.1029/JA091iA02p01651

Silwal, A., Gautam, S. P., Poudel, P., Karki, M., Adhikari, B., Chapagain, N. P., et al. (2021). Global positioning system observations of ionospheric total electron content variations during the 15th January 2010 and 21st June 2020 solar eclipse. *Radio Science*, *56*(5), e07215. https://doi.org/10.1029/2020RS007215

St.-Maurice, J. P., Ambili, K. M., & Choudhary, R. K. (2011). Local electrodynamics of a solar eclipse at the magnetic equator in the early afternoon hours. *Geophysical Research Letters*, *38*(4), L04102. https://doi.org/10.1029/2010GL046085

Sun, Y.-Y., Liu, J.-Y., Lin, C. C.-H., Lin, C.-Y., Shen, M.-H., Chen, C.-H., & Chou, M.-Y. (2018). Ionospheric bow wave induced by the moon shadow ship over the continent of United States on 21 August 2017. *Geophysical Research Letters*, *45*(2), 538–544. https://doi.org/10.1002/2017GL075926

Tian, Z., Sui, Y., Zhu, S., & Sun, Y.-Y. (2022). Enhancement of electron density in the ionospheric F_2 layer near the first contact of the total solar eclipse on 21 august 2017. *Earth and Space Science*, *9*(1), e02016. https://doi.org/10.1029/2021EA002016

Tomás, A. T., Lühr, H., FöRster, M., Rentz, S., & Rother, M. (2007). Observations of the low-latitude solar eclipse on 8 April 2005 by CHAMP. *Journal of Geophysical Research*, *112*(A6), A06303. https://doi.org/10.1029/2006JA012168

Vadas, S. L., & Liu, H.-l. (2009). Generation of large-scale gravity waves and neutral winds in the thermosphere from the dissipation of convectively generated gravity waves. *Journal of Geophysical Research*, *114*(A10), A10310. https://doi.org/10.1029/2009JA014108

Verhulst, T. G. W., & Stankov, S. M. (2018). Ionospheric wave signature of the American solar eclipse on 21 August 2017 in Europe. *Advances in Space Research*, *61*(9), 2245–2251. https://doi.org/10.1016/j.asr.2018.02.007

Wang, W., Dang, T., Lei, J., Zhang, S., Zhang, B., & Burns, A. (2019). Physical processes driving the response of the F_2 region ionosphere to the 21 August 2017 solar eclipse at Millstone Hill. *Journal of Geophysical Research: Space Physics*, *124*(4), 2978–2991. https://doi.org/10.1029/2018JA025479

Wu, C., Ridley, A. J., Goncharenko, L., & Chen, G. (2018). GITM-data comparisons of the depletion and enhancement during the 2017 solar eclipse. *Geophysical Research Letters*, *45*(8), 3319–3327. https://doi.org/10.1002/2018GL077409

Yan, M., Dang, T., Lei, J., Wang, W., Zhang, S.-R., & Le, H. (2021). From bow waves to traveling atmospheric disturbances: Thermospheric perturbations along solar eclipse trajectory. *Journal of Geophysical Research: Space Physics*, *126*(4), e28523. https://doi.org/10.1029/2020JA028523

Yau, A. W., Foss, V., Howarth, A. D., Perry, G. W., Watson, C., & Huba, J. (2018). Eclipse-induced changes to topside ion composition and field-aligned ion flows in the August 2017 solar eclipse: E-POP observations. *Geophysical Research Letters*, *45*(20), 10829–10837. https://doi.org/10.1029/2018GL079269

Zhai, C., Dang, T., Yao, Y., Kong, J., Chen, Y., & Cheng, X. (2023). Three-dimensional ionospheric evolution and asymmetry of the electron density depletion generated by the 21 June 2020 annular solar eclipse. *Journal of Geophysical Research: Space Physics*, *128*(12), e2023JA031725. https://doi.org/10.1029/2023JA031725

Zhang, S.-R., Erickson, P. J., Goncharenko, L. P., Coster, A. J., Rideout, W., & Vierinen, J. (2017). Ionospheric bow waves and perturbations induced by the 21 August 2017 solar eclipse. *Geophysical Research Letters*, *44*(24), 12067–12073. https://doi.org/10.1002/2017GL076054

Zhang, S.-R., Erickson, P. J., Vierinen, J., Aa, E., Rideout, W., Coster, A. J., & Goncharenko, L. P. (2021). Conjugate ionospheric perturbation during the 2017 solar eclipse. *Journal of Geophysical Research: Space Physics*, *126*(2), e28531. https://doi.org/10.1029/2020JA028531